Variations in the Raman peak shift as a function of hydrostatic pressure for various carbon nanostructures: A simple geometric effect

J. Sandler, M. S. P. Shaffer, and A. H. Windle
Department of Materials Science and Metallurgy, University of Cambridge, Cambridge CB2 3QZ, United Kingdom

M. P. Halsall
Department of Physics, UMIST, Manchester M60 1QD, United Kingdom

M. A. Montes-Morán, C. A. Cooper, and R. J. Young
Materials Science Centre, UMIST/University of Manchester, Manchester M1 7HS, United Kingdom
(Received 7 February 2002; revised 18 July 2002; published 27 January 2003)

We have investigated pressure-induced Raman peak shifts for various carbon nanostructures with distinct differences in the degree of structural order. The high-frequency tangential vibrational modes of the hollow nanostructures, as well as those of graphite crystals and a macroscopic carbon fiber used as reference materials, were observed to shift to higher wave numbers. The hollow nanostructures and the carbon fiber displayed two distinct pressure regimes with transition pressures between 0.75 and 2.2 GPa, whereas the graphite crystals showed a linear pressure dependence up to hydrostatic pressures of 5 GPa. The observed peak shifts were reversible for all hollow nanostructures and graphite. Although the pressure-induced Raman peak shift in the low pressure regime could be used to identify the elastic properties of the macroscopic carbon fiber, a theoretical model shows that the observed deviations in the pressure coefficients of the hollow nanostructures in this regime can be explained entirely on the basis of geometric effects. The close match of all Raman peak shifts in the high pressure regime indicates a reversible flattening of the nanostructures at the transition point.

DOI: 10.1103/PhysRevB.67.035417 PACS number(s): 78.30.Na, 61.46.+w, 62.50.+p, 81.07.De

I. INTRODUCTION

Both multi-wall (MWCNTs) and single-wall carbon nanotubes (SWCNTs) can be produced by a variety of processes such as carbon arc discharge,[1–3] laser vaporization,[4] and various chemical vapor deposition and catalytic growth processes.[5–8] SWCNTs grow mostly as bundles or ''ropes,'' containing between 20 and 100 individual tubes.[9,3,7] The quality and yield of carbon nanotubes depends on the synthesis technique and the specific growth conditions used. Catalytic processes generally involve lower growth temperatures and can lead to both variations in the orientation of the graphitic planes with respect to the tube axis and to an increased concentration of structural defects. However, catalytically-grown carbon nanostructures are typically available in larger quantities and may enable bulk applications in such areas as polymer nanocomposites. It is important to understand the structure-property relationships for carbon nanostructures so that a suitable material can be chosen for a given application.

The mechanical properties of carbon nanotubes have been predicted to be sensitive to details of structure,[10] an effect which has now been established experimentally.[11] It was discovered that point defects hardly affect the elastic properties of MWCNTs, although more general structural disorder can reduce the elastic modulus by orders of magnitude.[11] Heat treatment of catalytically grown MWCNTs led to an increase in the elastic stiffness by at least one order of magnitude.[11] Despite recent experimental advances in probing individual mechanical nanotube properties based on *in situ* tensile tests,[12,13] we are still lacking a fundamental understanding of the structure-property relationships for the wide variety of nanostructures currently available. Microscopic tests on individual carbon nanotubes are difficult to perform, time consuming, and a statistically significant experimental analysis of the mechanical properties of different nanostructures remains challenging.

It has been shown that laser Raman spectroscopy can be applied to follow the deformation of carbon fibers as a function of applied strain.[14–17] The tangential Raman E_{2g_2} mode shifts to lower wave numbers under an applied uniaxial tensile strain and to higher wave numbers upon axial compression. The rate of the shift per unit strain in such experiments was found to be proportional to the Young's modulus of the carbon fiber.

Optical spectroscopy, in particular laser Raman spectroscopy, can be employed to study the vibrational properties of carbon nanotubes. In recent years *in situ* comparative Raman studies of nanotubes and graphite under hydrostatic pressure[18–24] have been performed in addition to x-ray pressure studies[25,18,26–28] as well as neutron diffraction studies.[29] In a detailed study of the pressure dependence of the tangential modes of laser-grown SWCNTs in the pressure range up to 5 GPa Peters *et al.*[22] observed a clear transition of all three modes around 1.7 GPa, as well as a deteriorating radial breathing mode around this pressure. Providing additional molecular dynamic simulations of the lattice constants of (10,10) armchair SWCNT bundles as a function of pressure, they concluded that the nanotubes undergo a structural phase transition from a circular to an oval cross section at this pressure.[22] Tight-binding total energy calculations by Kahn and Lu[30] of peak position vs pressure for the three modes in (10,10) tubes showed good agreement with the experimental

TABLE I. List of the carbon structures investigated, their abbreviations and symbols used throughout this study, and their dimensions determined from electron microscopy.

Material	Abbrev.	Symbol	Outer diameter [nm]	Wall thickness [nm]
Graphite crystals	Graphite	■	N.A.	N.A.
Vapor-grown nanofibers	VGCNF	◇	155±30	42±7
As-received catalytically-grown multi-wall nanotubes	C-MWCNT	▼	10.4±3.3	4.1±1.8
Graphitized catalytically-grown multi-wall nanotubes	G-MWCNT	▽	10.4±3.3	4.1±1.8
Laser-grown single-wall nanotubes	SWCNT	● and ○	1.54	0.34[a]
Arc-grown multi-wall nanotubes	A-MWCNT	△	15.1±2.6	5.5±2.6
High-modulus carbon fiber	*P*100	⋆	10 000±1000	N.A.

[a]For explanation of SWCNT dimensions see text.

slopes, transition pressure, and type of structural deformation. Two studies comparing linearly fitted pressure coefficients for SWCNTs and MWCNTs up to pressures of 10 GPa showed a slightly smaller pressure dependence for the MWCNTs.[21,23] This effect was explained on the basis of a simple elasticity approach, considering nanotubes to be hollow cylinders made up of mechanically isotropic sheets.[21] Recently, excellent agreement between *ab initio* calculations and an elastic continuum approximation has been shown for individual SWCNTs in a bundle under hydrostatic pressure.[31]

We report here a comparative study of pressure-induced shifts of the high-frequency tangential Raman modes for a range of different carbon nanostructures, graphite crystals, and a macroscopic carbon fibre as a function of hydrostatic pressure up to 5 GPa. The aim was to distinguish the elastic properties of these nanostructures as a function of their degree of structural disorder by the variations in the pressure-induced peak shifts. We have observed a transition in the pressure dependence for all hollow nanostructures and the macroscopic carbon fiber and explain their relative behaviors in the identified different regimes. A theoretical model is applied to predict the pressure-induced high-frequency Raman peak shifts for all nanostructured materials in the low-pressure regime and the calculated results are compared to the experimentally observed pressure coefficients.

II. MATERIALS AND EXPERIMENTAL DETAILS

The materials used in this study were vapor-grown carbon nanofibers (VGCNF) (Applied Sciences Inc., USA), arc-grown multi-wall carbon nanotubes (A-MWCNT) (Technical University Hamburg-Harburg, Germany), catalytically-grown multi-wall carbon nanotubes (C-MWCNT) (Hyperion Catalysis International, USA), and laser-grown single-wall carbon nanotubes (SWCNT) (Tubes@Rice, USA). Graphite crystals (Graphite, Fluka Chemie AG, Switzerland) and a high-modulus mesophase pitch carbon fiber (P100, BP Amoco, USA) were investigated as reference materials. Both transmission and scanning electron microscopy were used to determine the average diameter and wall thickness of all the hollow carbon nanostructures, to assess their structural arrangements, and to confirm that the ends were closed. The materials used in this study are listed in Table I as well as results of the geometric analysis.

The carbon nanofiber material consists of a mixture of two distinctive structures present in the sample, relatively straight cylindrical tubes and the so-called bamboo tubelike structures, arranged into loose aggregates. The inner part of a nanofiber wall shows an arrangement of the graphitic layers at a $\pm 15°$ angle with regard to the fiber axis. The outside part of the wall is made up of short graphitic segments parallel to the fiber axis.

The arc-grown multi-wall carbon nanotubes, taken from the core of the arc deposit, are long and straight cylindrical tubes. On the other hand, the catalytically-grown multi-wall carbon nanotubes, generated by decomposition of hydrocarbon gases,[32] consist, almost exclusively, of balls of loosely aggregated nanotubes that are noncoiled but generally curved and kinked as a result of structural defects.[33] In order to minimize these structural defects without changing the geometry of the tubes, a sample of C-MWCNT was graphitized at 2800 °C in an inert atmosphere; this sample is labeled G-MWCNT. This type of treatment is well known to improve the crystalline quality of defective nanotubes.[11]

The SWCNTs were prepared by a pulsed-laser vaporization process.[4] The typical narrow diameter distribution of individual tubes in the bundles has been determined from transmission electron microscopy, x-ray diffraction, and Raman spectroscopy to be around 1.2 nm.[4] It has been pointed out that more accurate processing of experimental data can be achieved by accounting for the discrete nature of the cross section of a single-wall nanotube by increasing the outer radius of such a tube by half the interatomic graphite sheet spacing.[34] Furthermore, all-electron *ab initio* calculations of a SWCNT and a graphene layer have shown that their effective wall thickness should relate to the van der Waals radius for carbon, and hence have a value of 0.34 nm.[35] Scaling the wall thickness of a single-wall nanotube to the graphite interlayer spacing of 0.34 nm leads to an effective outer diameter of 1.54 nm, as given in Table I.

All Raman spectra were recorded at room temperature using a Renishaw 1000 Raman microprobe system. Scattered light from the sample was collected in the backscattering geometry, passed through a holographic notch filter and a diffraction grating and was detected with a Peltier cooled charge coupled device (CCD) camera. Initial high-frequency

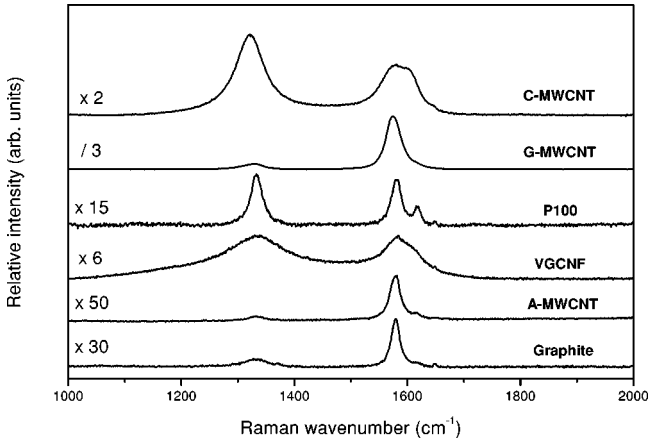

FIG. 1. Comparative high-frequency Raman spectra of graphite crystals, arc-grown multi-wall carbon nanotubes (A-MWCNTs), vapor-grown carbon nanofibers (VGCNFs), as-received catalytically-grown carbon nanotubes (C-MWCNTs), and annealed catalytically-grown nanotubes (G-MWCNTs) taken in air for a random orientation within the samples. In addition, the Raman spectra of a high-modulus carbon fiber ($P100$) is shown, the laser polarized parallel to the fiber axis in this case. All spectra are normalized with regard to the G-band intensity, the scaling factor is indicated.

Raman spectra in air of the as-supplied materials were obtained using 514.5 nm excitation of a 50 mW argon laser with the incident and backscattered laser light polarized parallel. The ratio of the relative intensities of the D and G bands was taken as a quantitative measure of the degree of structural order and was compared to high-resolution TEM images. For these measurements only the macroscopic carbon fiber was positioned parallel to the laser polarization whereas all other samples had a random orientation with regard to the incident light.

The high-pressure Raman measurements were performed in a gasketed diamond anvil cell (DAC) (Mao-Bell type) with a 4:1 mixture by volume of methanol-ethanol as the pressure transmitting medium. A small chip of ruby was also placed in the 40 μm diameter sample chamber. The ruby fluorescence method allows the calibration of the pressure to within 3% following the R-line emission.[36] All pressure cell measurements were also carried out at room temperature in a backscattering geometry with the incident and backscattered laser light polarized parallel. A $\times 20$ microscopic lens was used to focus the laser beam on the sample inside the pressure cell. The pressure cell was positioned in such a way that the macroscopic carbon fiber axis was parallel to the laser polarization. All other samples had a random orientation within the pressure gasket and in these cases the laser sampled a number of randomly oriented nanostructures.

The increasing pressure within the cell was calibrated with the 633 nm line of a 25 mW He-Ne laser. In order to obtain a clear signal from the graphitic materials without exciting the ruby, a 50 mW 780 nm near-IR excitation was then used to follow the characteristic high-frequency tangential Raman modes of the carbon samples at different locations within the cell as a function of the applied hydrostatic pressure. Static scans were centered around 1580 cm^{-1} in order to prevent saturation of the CCD camera from the strong diamond peak. Depending on the crystalline quality of the sample the integration time had to be varied between 1 and 5 min.

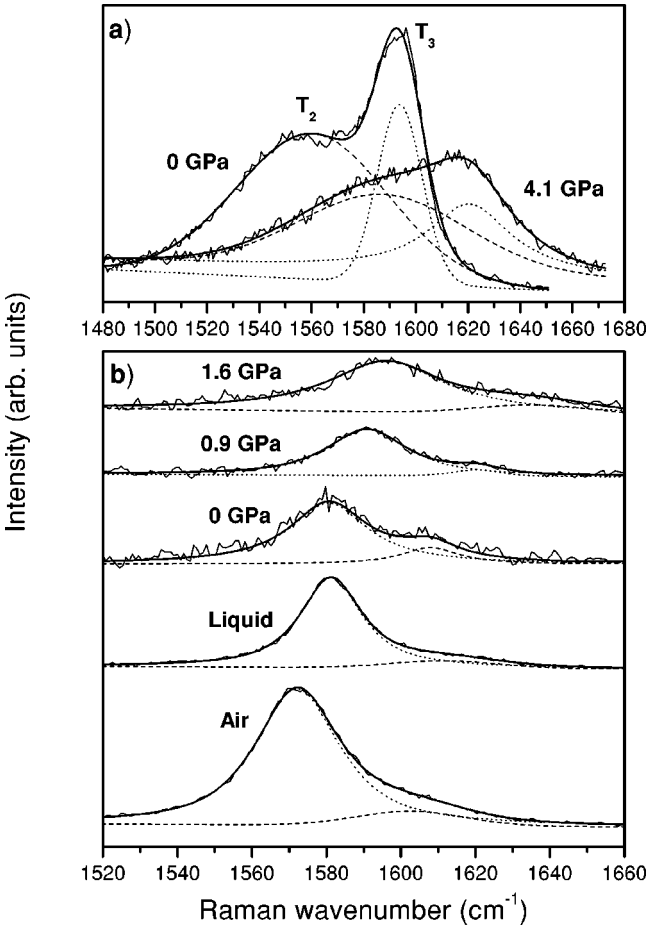

FIG. 2. Line-shape analysis of the high-frequency Raman spectra of (a) laser-grown SWCNT inside the pressure cell at zero and 4.1 GPa applied pressure (the two observed modes are labeled T_2 and T_3) and (b) arc-grown multi-wall nanotubes in air, immersed in the pressure transmitting medium, upon closure of the pressure cell, and as a function of increasing pressure.

Prior to closure of the pressure cell high-frequency Raman spectra of all samples immersed in the pressure transmitting medium were recorded. The ruby calibration for these measurements still showed zero pressure. All high-frequency peak values were determined by fitting the raw data from the spectrometer with a mixture of Lorentzian and Gaussian routines. For all graphitic samples the presence of the feature at ~ 1620 cm^{-1} (D'-band) was also taken into account and fitted with the same routine.

III. RESULTS

High-frequency Raman spectra taken in air revealed differences in the degree of structural perfection of the investigated materials, as shown in Fig. 1. All materials exhibited two main features at about 1350 and ~ 1580 cm^{-1}, respectively, the former corresponding to the defect-induced Ra-

TABLE II. Summary of the experimentally observed shifts due to immersion in the pressure liquid and resulting peak position at zero GPa hydrostatic pressure. The experimental pressure coefficients for both regimes before and after the transition pressure are given as well as the theoretical pressure coefficients calculated up to the experimental transitions.

Material	$d\omega_{\text{liquid}}$ [cm^{-1}]	ω_0 [cm^{-1}] (Closed cell)	$d\omega_{\text{experiment}}/dp$ [cm^{-1}/GPa] (Before transition)	$d\omega_{\text{experiment}}/dp$ [cm^{-1}/GPa] (After transition)	$d\omega_{\text{theory}}/dp$ [cm^{-1}/GPa] (Up to transition)
Graphite	~4	1581	4.6		4.5
VGCNF	~6	1597	7.8	4.3	7.5
C-MWCNT	~5	1603	6.3	4.1	6.6
G-MWCNT	~5	1577	6.3	4.3	6.5
SWCNT T_3	not meas.	1594	9.7	5.3	9.6
SWCNT T_2	not meas.	1552	8.0	4.3	9.9
A-MWCNT	~10	1582	11.9	4.4	5.4
*P*100 (*G* band)		1582	7.0	3.7	4.5
*P*100 (*D'* band)		1613	7.1	3.7	4.5

man *D* band and the latter to the graphite in-plane vibration mode called *G* band.[37] In addition, the feature at ~1620 cm^{-1} which is due to the maximum in the phonon density of states[38] was observable and was most prominent for the macroscopic carbon fiber with the axis parallel to the laser light polarization.

The high-frequency modes of the laser-grown SWCNTs inside the closed pressure cell at 0 and 4.1 GPa hydrostatic pressure are shown in Fig. 2(a). The solid lines represent the curve fits obtained from the mixed Lorentzian and Gaussian line-shape analysis. We could only clearly identify two peaks in the tangential mode region which we labeled T_2 for the peak at 1552 and T_3 for the one at 1594 cm^{-1}, according to Venkateswaran *et al.*[20] Taking into account the distribution of helicities and diameters present in these nanotube bundles both high-frequency modes should have contributions from E_{2g}, E_{1g}, and A_{1g} vibrations. Figure 2(b) shows the measured high-frequency spectrum and the corresponding line-shape analysis of the A-MWCNT sample at different stages of the experiment as an example. It can clearly be seen that the immersion of nanotubes in the liquid shifted the position of both the *G* band and the *D'* band to higher wave numbers and slightly reduced the intensity. The obtained peak shifts $d\omega_{\text{liquid}}$ due to the liquid for the *G* band of all investigated materials are displayed in Table II, as well as the resulting peak positions ω_0 at zero pressure. (This effect could not be established for the SWCNT material since it was delivered in a surfactant solution and no spectrum in air without possible effects of the surfactant could be taken.) The next spectrum taken upon closure of the cell and the ruby calibration showing zero hydrostatic pressure reveals that the *G* band remained at that position. Due to the presence of the diamond window the noise level increased but the *G* band and its position could clearly be detected.

With increasing hydrostatic pressure the high-frequency peaks of all carbon nanostructures were found to shift to higher wave numbers, which corresponds to a reduction in bond length and associated stiffening of the bonds. We observed a broadening of the tangential modes for all graphitic samples. A comparative plot of the observed Raman high-frequency peak positions of all investigated carbon structures as a function of hydrostatic pressure is shown in Fig. 3. The lines represent linear fits to the obtained data points and the arrows indicate transitions in the pressure coefficients. For the SWCNT sample both tangential modes are shown.

It can be seen in Fig. 3(a) that the graphite *G* band shows a linear pressure dependence over the investigated pressure range up to 5 GPa. In contrast, the macroscopic carbon fiber clearly reveals two distinct regimes with a transition around 0.75 GPa. Both the *G* band and the *D'* band feature of this sample show identical pressure-induced peak shifts and the transition occurring at the same pressure. During the experiment the carbon fiber was clearly visible in the pressure cell up to the transition pressure where it was observed to break up into smaller fragments.

All of the hollow nanostructures also display two distinct regimes with a transition pressure that varies for the different materials as shown in Figs. 3(b) and 3(c) (the graphite data is included for comparison). An initial steeper slope gives way to a shallower slope that lies approximately parallel to the graphite line at higher pressures. The experimentally observed pressure dependencies $d\omega_{\text{experiment}}/dp$, in both regimes, are listed for all materials in Table II.

It is interesting to note that the initial slopes and the transition pressures vary for the different types of multi-wall carbon nanotubes such as the arc-grown and the catalytic material, as well as the vapor-grown carbon nanofibers. On the other hand, the defective and graphitized catalytic nanotubes with identical geometries show identical pressure dependencies both below and above the transition and the same transition pressure. Above the transition point, the pressure coefficients of all hollow nanostructure modes, except the T_3 SWCNT mode, are slightly lower than the one obtained for graphite. In addition, the two tangential SWCNT modes diverge, the T_3 mode showing a higher pressure coefficient in both regimes. The shifts in peak position were observed to be fully reversible for all hollow nanostructures and graphite, over the pressure range that was investigated.

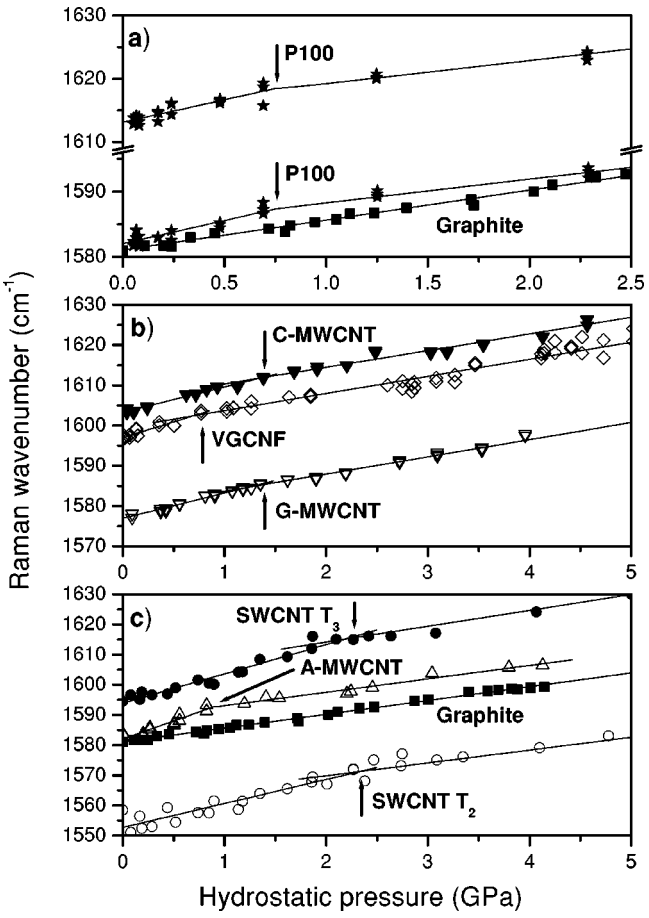

FIG. 3. Comparative plot of the Raman high-frequency peak positions for (a) graphite and high-modulus carbon fiber ($P100$), (b) vapor-grown carbon nanofibers, as-received and graphitized catalytic multi-wall carbon nanotubes, and (c) graphite, arc-grown multi-wall carbon nanotubes, and laser-grown single-wall nanotubes as a function of hydrostatic pressure. The lines represent best fits and the arrows indicate the transition pressures. Note that for the carbon fiber the shift for the D' band is included in (a).

IV. DISCUSSION

The observed variations in the high-frequency peak positions at ambient pressure for a given laser excitation for the different carbon nanostructures verify our electron microscopy observations with regard to the differences in structural perfection. The Raman features of graphitic materials in this frequency range are sensitive to structural sample quality[38] with the G band depending on the two-dimensional graphite ordering, whereas nonplanar microstructural distortions contribute to the D band. The change in Raman spectra with heat treatment of the catalytic multi-wall carbon nanotubes clearly reveals improved structural perfection, as has been shown for vapor-grown carbon nanofibers.[39]

In addition to the variation in initial peak position we noticed a shift to higher wave numbers upon immersion of the nanoscale materials in the pressure medium. This shift has previously been ascribed to the cohesive energy density (CED) of the liquid, where the molecular forces induce a hydrostatic pressure on the suspended nanoscale particles.[40,41] We also observed such a shift when the nanoscale materials were immersed in the medium but did not find this shift to increase further upon closing the pressure cell, with the ruby calibration initially showing zero hydrostatic pressure. It is interesting to note that the macroscopic carbon fiber did not reveal any peak shift upon immersion in the pressure medium. Following the approach published by Wood *et al.*[41] the CED of the pressure medium used in this study can be expressed as a hydrostatic pressure of about 0.84 GPa. The experimentally obtained peak shifts due to the liquid are in good agreement with the pressure dependencies measured up to the transition points.

There is a linear increase in the E_{2g_2} peak position of graphite up to pressures of 5 GPa. The slope $d\omega/dp$ in our study is 4.6 cm^{-1}/GPa and compares well to the slope of 4.7 found by Hanfland *et al.*[18] Our results for the hollow nanostructures also closely match the literature. Both the initial higher pressure dependencies as well as the transition pressures of the SWCNTs agree with both experiment[22] and theory.[30] In the previous cases where transitions of the high-frequency modes at low pressures were not observed, possibly due to widely spaced data points, the slopes reported for both single-wall nanotubes[19,21,42,24,23] as well as multi-wall nanotubes[21,23] match those found in our higher pressure regime. From these slopes it appears that the pressure dependence of the tangential Raman modes is generally smaller for MWCNTs than for SWCNTs, as previously shown.[21,23]

In addition, we have observed a fully reversible pressure dependence for all our nanostructures over the pressure range investigated. In the case of all hollow materials the pressure-induced peak shift was found to follow the two slopes with no apparent time dependence. Within experimental error, the transitions occurred at the same pressure for both loading and unloading cycles. Raman spectra taken in air after the pressure run showed identical high-frequency modes compared to spectra taken before the pressure cell experiment. Furthermore, SEM analysis of the carbon nanofibers after the pressure experiment showed no change in structure. These results are consistent with studies that found that the Raman high-frequency mode shifts could be reversed upon release of the pressure, including those which observed a clear transition in the pressure dependence. Peters *et al.*[22] reported a small time dependence but did not explore the effect quantitatively.

In the case of the solid macroscopic carbon fiber the higher initial pressure dependence compared to the graphite crystals is related to the lower stiffness of the material. Taking the elastic in-plane stiffness of ideal graphite to be 1.06 TPa, the ratio of the initial slope of the P100 fiber compared to the one for graphite results in an elastic modulus of about 700 GPa for the carbon fiber. This result is in excellent agreement with values obtained for this fiber from uniaxial tensile and bending tests and the manufacturer's data. The Raman peak shift was found to be irreversible in this case which can be explained by a shattering of the fiber observed after the pressure run.

V. THEORETICAL APPROACH

From the higher initial pressure dependence of the high-modulus carbon fiber in our experiment one would assume

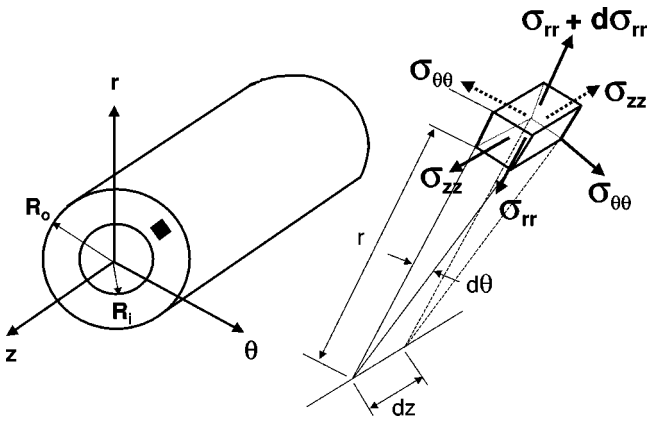

FIG. 4. Model of thick-walled cylinder under hydrostatic pressure and the coordinates used. The volume element displays the normal stresses which, in the absence of shear, are a function of the radial coordinate r only.

that a higher Raman peak shift per unit stress indicates higher in-plane strains and, therefore, a more compliant material. Nevertheless, the identical pressure dependencies of both the untreated and the graphitized catalytically-grown carbon nanotubes (same diameter but higher stiffness) are strong evidence that the deviations in initial pressure coefficients of all hollow nanostructures are related more strongly to the geometry of the nanoscale samples and not variations in elastic properties. Furthermore, the very high pressure coefficient (high compliance) of the arc-grown multi-wall carbon nanotubes compared to the other materials would otherwise be surprising since such nanotubes show very little structural disorder.

To test the hypothesis that the observed initial pressure coefficients of the hollow nanostructures are related to the geometry rather than variations in stiffness, we have calculated the expected Raman shifts for ideal graphite as a solid and arranged in a cylindrical geometry equivalent to each of the hollow nanomaterials tested. We approximate all hollow nanostructures by a thick-walled cylinder with a wall of finite thickness and closed ends. The pressure inside the closed nanostructures is assumed to be zero. Even atmospheric pressure within the nanotubes is orders of magnitude smaller than the imposed hydrostatic pressure and can therefore be neglected.

The equations for a thick-walled cylinder under hydrostatic pressure are applicable to locations far from the tube ends that make up the majority of the samples. Since only axially symmetrical loads and constraints are admitted, the solution is axially symmetrical. We use cylindrical coordinates r, θ, and z for the radial, circumferential, and axial directions, respectively. The nonzero stress components are principal stresses σ_{rr}, $\sigma_{\theta\theta}$, and σ_{zz}. Figure 4 shows the definition of coordinates and the stresses acting on a volume element of the cylinder wall.

In the absence of a temperature change and an internal pressure the following expressions for the stress components on the surface of a closed cylinder can be derived:[43]

$$\sigma_{rr}=\frac{R_i^2-R_o^2}{R_o^2-R_i^2}\ p, \tag{1}$$

$$\sigma_{\theta\theta}=\frac{-R_i^2-R_o^2}{R_o^2-R_i^2}\ p,$$

$$\sigma_{zz}=\frac{-R_o^2}{R_o^2-R_i^2}\ p,$$

where R_i and R_o are the inner and outer radii of the cylinder, respectively, and p is the hydrostatic pressure.

These principal stresses can be transformed into in-plane strain deformations of the ideal graphitic cylinder in the axial ϵ_{xx} and circumferential ϵ_{yy} directions by using the elastic compliances of ideal graphite

$$\epsilon_{xx}=S_{11}\sigma_{zz}+S_{12}\sigma_{\theta\theta}+S_{13}\sigma_{rr}, \tag{2}$$

$$\epsilon_{yy}=S_{12}\sigma_{zz}+S_{11}\sigma_{\theta\theta}+S_{13}\sigma_{rr}.$$

The elastic compliances S are taken as $S_{11}=0.98$, $S_{12}=-0.16$, and $S_{13}=-0.33$ GPa^{-1} (Ref. 44) and the dimensions of all materials are as listed in Table I.

Sakata *et al.* have measured the strain dependent Raman E_{2g_2} mode for highly graphitized vapor-grown carbon fibers during uniaxial tensile testing.[45] From the observed polarization dependent frequency shifts they have derived phenomenological coefficients which describe the changes in the elastic constants of the $k\approx 0$ optical phonons with strain.

Following their approach we can estimate the polarization dependent Raman peak position as a function of the hydrostatic pressure-induced in-plane strains as follows:

$$\omega_{\text{parallel}}=\omega_0+\left(\frac{1}{2\omega_0}\right)[(A+B)\epsilon_{xx}+(A-B)\epsilon_{yy}],$$

$$\omega_{\text{perpendicular}}=\omega_0+\left(\frac{1}{2\omega_0}\right)[(A-B)\epsilon_{xx}+(A+B)\epsilon_{yy}]. \tag{3}$$

Here ω_0 is the experimentally observed peak position inside the pressure cell at zero hydrostatic pressure, and A and B are the derived phenomenological coefficients with values $A=-1.44\times 10^7$ and $B=\pm 5.8\times 10^6$ cm^{-2}.[45] The subscripts denote the orientation of the cylinder axis with regard to the polarization of the incident laser light. Taking a mean of the two polarization dependent peak shifts to account for the random arrangement of the nanoscale samples in the pressure cell allows us to calculate the Raman peak shift as a function of hydrostatic pressure. A comparative plot of the experimental data points in the pressure regime below the transition points and the theoretical predictions (solid lines) is shown in Fig. 5.

Without the introduction of any arbitrary fitting parameters there is a close match between our theoretical predictions and the experimental slopes for all nanoscale materials, except the arc-grown multi-wall carbon nanotubes. The theoretically calculated Raman peak shifts $d\omega_{\text{theory}}/dp$ and the starting position of the tangential modes inside the pressure cell ω_0 used for the calculations are included in Table II. For the solid graphite crystals there is a perfect match of the

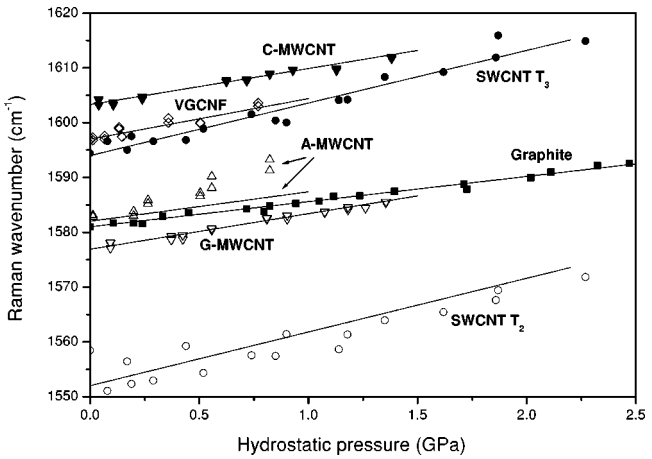

FIG. 5. Comparison of experimental data (symbols) and theoretical predictions (solid lines) for the Raman peak shifts in the low pressure regime for graphite, arc-grown multi-wall nanotubes, vapor-grown nanofibers, defective and annealed catalytically-grown multi-wall nanotubes, and laser-grown single-wall nanotubes as a function of hydrostatic pressure.

hydrostatic pressure induced E_{2g_2} peak shift. The underestimation of the pressure dependence of the arc-grown nanotubes in our model relates to a reduction in the effective wall thickness. TEM analysis has revealed that for these nanotubes some of the inner shells are essentially isolated from the hydrostatic pressure due to premature closure within the outer shell. The estimated wall thickness in our model is based on the wall thickness in the middle of the tube which, therefore, does not represent the true load bearing geometry. An effective wall thickness of 2.8 nm which is about 1/2 of the one obtained from the TEM observations yields a theoretical prediction matching the experimental data.

We have followed our approach to calculate both high-frequency SWCNT modes as a function of pressure. A good fit to the experimental data can be observed for the T_3 mode. The slight overestimation of the T_2 mode might be due to more pronounced contributions of other atomic vibrations. SWCNT axial and circumferential vibrations have been predicted theoretically to show different pressure induced derivatives depending on chirality.[46]

It must be noted that our theoretical calculations are only relevant at pressures up to the experimentally observed transition points. We believe that at this pressure a reversible flattening occurs. Molecular dynamics studies of SWCNTs as a function of hydrostatic pressure have demonstrated that a nanotube at the critical pressure will abruptly release energy by locally switching into a different morphology.[47] Although it cannot be resolved in our experiment such a collapse cannot occur simultaneously throughout a nanotube of substantial length.[48] In the hydrostatic case a reversible collapse is initiated locally and then propagates with a speed proportional to the square root of overpressure $v \approx (p/p_0 - 1)^{1/2}$ along the tube.[48] Similar abrupt transitions have also been observed in simulations of SWCNTs subjected to various mechanical deformations.[49–51]

In the high pressure regime after this transition large portions of the nanotube walls are approximately parallel so that the pressure dependence of this structure is expected to resemble bulk graphite, in agreement with our experimental results. The slight variations in final pressure coefficients are related to the covalent bonds between the graphene layers that are not present in the graphite crystals. To estimate the exact collapse pressure, the anisotropy of graphite needs to be considered. A simple continuum elasticity estimation of the collapse pressure based on the in-plane stiffness of an ideal graphene layer does not seem applicable.

VI. CONCLUSIONS

We have followed the high-frequency tangential Raman modes of various carbon nanostructures as a function of hydrostatic pressure to investigate the elastic properties of bulk samples with distinct variations in the degree of structural order. The Raman modes were found to shift reversibly to higher wave numbers with increasing pressure and to fall into two distinct linear regimes for all hollow nanostructures. Taking into account the polarization dependence of a strain-induced Raman peak shift we are able to predict the initial pressure dependence of all the nanostructures tested. The variations in initial pressure coefficients are based purely on geometric differences, with the in-plane strains at a nanotube surface dependent on the diameter and the effective load carrying wall thickness. These differences in in-plane strains as a function of hydrostatic pressure can be calculated by a simple continuum model. Nevertheless, the initial pressure-induced Raman peak shift could be used to identify the elastic properties of a macroscopic carbon fiber. We attribute the change in slope for the hollow nanostructures to a reversible collapse transition. We are currently evaluating whether the differences in collapse points or the initial Raman peak shifts upon immersion in a liquid can be linked to variations in intrinsic elastic properties.

This study also highlights the need to take overall nanotube geometry into account when assessing their mechanical performance rather than simply referring to the intrinsic stiffness of the walls, and provides evidence that continuum mechanics can be applied at very small size scales under certain circumstances, in agreement with earlier theoretical predictions for carbon nanotubes.[52]

ACKNOWLEDGMENTS

Thanks to S. Friend of Hyperion Catalysis for making possible this work on their catalytically-grown material. The authors would also like to acknowledge Applied Sciences Inc. for providing the vapor-grown carbon nanofibers used in this study. Thanks for support goes to the Cambridge European Trust and the EPSRC. We also gratefully acknowledge financial support from the European Thematic Network CNT-NET (Grant No. G5RT-CT-2001-05026).

[1] T.W. Ebbesen and P.M. Ajayan, Nature (London) **358**, 220 (1992).
[2] D.T. Colbert, J. Zhang, S.M. McClure, P. Nikolaev, Z. Chen, J.H. Hafner, D.W. Owens, P.G. Kotula, C.B. Carter, J.H. Weaver, A.G. Rinzler, and R.E. Smalley, Science **266**, 1218 (1994).
[3] C. Journet, W.K. Maser, P. Bernier, A. Loiseau, M. Lamy de la Chapelle, S. Lefrant, P. Deniard, R. Lee, and J.E. Fischer, Nature (London) **388**, 756 (1997).
[4] A.G. Rinzler, J. Liu, H. Dai, P. Nikolaev, C.B. Huffman, F.J. Rodríguez–Maćias, P.J. Boul, A.H. Lu, D. Heyman, D.T. Colbert, R.S. Lee, J.E. Fischer, A.M. Rao, P.C. Eklund, and R.E. Smalley, Appl. Phys. A: Mater. Sci. Process. **67**, 29 (1998).
[5] M. Endo, K. Takeuchi, S. Igarashi, K. Kobori, M. Shirais, and H.W. Kroto, J. Phys. Chem. Solids **54**, 1841 (1993).
[6] C.N.R. Rao, A. Govindaraj, R. Sen, and B.C. Satishkumar, Mater. Res. Innovations **2**, 128 (1998).
[7] H.M. Cheng, F. Li, G. Su, H.Y. Pan, L.L. He, X. Sun, and M.S. Dresselhaus, Appl. Phys. Lett. **72**, 3282 (1998).
[8] R. Andrews, D. Jacques, A.M. Rao, F. Derbyshire, D. Qian, X. Fan, E.C. Dickey, and J. Chen, Chem. Phys. Lett. **303**, 467 (1999).
[9] A. Thess, R. Lee, P. Nikolaev, H. Dai, P. Petit, J. Robert, C. Xu, Y.H. Lee, S.G. Kim, A.G. Rinzler, D.T. Colbert, G.E. Scuseria, D. Tománek, J.E. Fischer, and R.E. Smalley, Science **273**, 483 (1996).
[10] O. Zhou, R.M. Fleming, D.W. Murphy, C.H. Chen, R.C. Haddon, A.P. Ramirez, and S.H. Glarum, Science **263**, 1744 (1994).
[11] J.-P. Salvetat, A.J. Kulik, J.-M. Bonnard, G.A.D. Briggs, T. Stökli, K. Méténier, S. Bonnamy, F. Béguin, N.A. Burnham, and L. Forró, Adv. Mater. **11**, 161 (1999).
[12] M.-F. Yu, B.I. Yakobson, and R.S. Ruoff, J. Phys. Chem. B **104**, 8764 (2000).
[13] M.-F. Yu, O. Lourie, M.J. Dyer, K. Moloni, T.F. Kelly, and R.S. Ruoff, Science **287**, 637 (2000).
[14] I.M. Robinson, M. Zakikhani, R.J. Day, R.J. Young, and C. Galiotis, J. Mater. Sci. Lett. **6**, 1212 (1987).
[15] C. Galiotis and D.N. Batchelder, J. Mater. Sci. Lett. **7**, 545 (1988).
[16] Y. Huang and R.J. Young, J. Mater. Sci. Lett. **29**, 4027 (1994).
[17] M.A. Montes-Morán and R.J. Young, Carbon **40**, 857 (2002).
[18] M. Hanfland, H. Beister, and K. Syassen, Phys. Rev. B **39**, 12 598 (1989).
[19] A.K. Sood, P.V. Teredesai, D.V.S. Muthu, R. Sen, A. Govindaraj, and C.N.R. Rao, Phys. Status Solidi B **215**, 393 (1999).
[20] U.D. Venkateswaran, A.M. Rao, E. Richter, M. Menon, A. Rinzler, R.E. Smalley, and P.C. Eklund, Phys. Rev. B **59**, 10 928 (1999).
[21] C. Thomsen, S. Reich, H. Jantoljak, I. Loa, K. Syassen, M. Burghard, G.S. Duesberg, and S. Roth, Appl. Phys. A: Mater. Sci. Process. **69**, 309 (1999).
[22] M.J. Peters, L.E. McNeil, J.P. Lu, and D. Kahn, Phys. Rev. B **61**, 5939 (2000).
[23] U.D. Venkateswaran, E.A. Brandsen, U. Schlecht, A.M. Rao, E. Richter, I. Loa, K. Syassen, and P.C. Eklund, Phys. Status Solidi B **223**, 225 (2001).
[24] P.V. Teredesai, A.K. Sood, S.M. Sharma, S. Karmakar, S.K. Sikka, A. Govindaraj, and C.N.R. Rao, Phys. Status Solidi B **223**, 479 (2001).
[25] Y.X. Zhao and I.L. Spain, Phys. Rev. B **40**, 993 (1989).
[26] T. Yagi, W. Utsumi, M.A. Yamakata, T. Kikegawa, and O. Shimomura, Phys. Rev. B **46**, 6031 (1992).
[27] L.-C. Chen, L.-J. Wang, D.-S. Tang, S.-S. Xie, and C.-Q. Jin, Chin. Phys. Lett. **18**, 577 (2001).
[28] J. Tang, L.-C. Qin, T. Sasaki, M. Yudasaka, A. Matsushita, and S. Iijima, Phys. Rev. Lett. **85**, 1887 (2000).
[29] S. Rols, I.N. Gontcharenko, R. Almairac, J.L. Sauvajol, and I. Mirebeau, Phys. Rev. B **64**, 1534011 (2001).
[30] D. Kahn and J.P. Lu, Phys. Rev. B **60**, 6535 (1999).
[31] S. Reich, C. Thomsen, and P. Ordejón, Phys. Rev. B **65**, 1534071 (2002).
[32] Hyperion Catalysis Inc., U.S. Patent 5,165,909, 1992.
[33] M.S.P. Shaffer, X. Fan, and A.H. Windle, Carbon **36**, 1603 (1998).
[34] S. Govindjee and J.L. Sackman, Solid State Commun. **110**, 227 (1999).
[35] G.V. Lier, C.V. Alsenoy, V.V. Doren, and P. Geerlings, Chem. Phys. Lett. **326**, 181 (2000).
[36] A. Jayaraman, Rev. Sci. Instrum. **57**, 1013 (1986).
[37] F. Tuinstra and J.L. Koenig, J. Chem. Phys. **53**, 1126 (1970).
[38] R. Saito, G. Dresselhaus, and M. S. Dresselhaus, *Physical Properties of Carbon Nanotubes* (Imperial College Press, London, 1998).
[39] M. Endo, K. Nishimura, Y.A. Kim, K. Hakamada, T. Matushita, M.S. Dresselhaus, and G. Dresselhaus, J. Mater. Res. **14**, 4474 (1999).
[40] J.R. Wood, M.D. Frogley, E.R. Meurs, A.D. Prins, T. Peijs, D.J. Dunstan, and H.D. Wagner, J. Phys. Chem. B **103**, 10 388 (1999).
[41] J.R. Wood, M.D. Frogley, A.D. Prins, D.J. Dunstan, and H.D. Wagner, High Press. Res. **18**, 153 (2000).
[42] P.V. Teredesai, A.K. Sood, D.V.S. Muthu, R. Sen, A. Govindaraj, and C.N.R. Rao, Chem. Phys. Lett. **319**, 296 (2000).
[43] A. P. Boresi, R. J. Schmidt, and O. M. Sidebottom, in *Advanced Mechanics of Solids*, 5th ed. (Wiley, New York, 1993), Chap. The thick–wall cylinder.
[44] B. T. Kelly, in *Physics of Graphite* (Applied Science, London, 1981).
[45] H. Sakata, G. Dresselhaus, M.S. Dresselhaus, and M. Endo, J. Appl. Phys. **63**, 2769 (1988).
[46] S. Reich, H. Jantoljak, and C. Thomsen, Phys. Rev. B **61**, 13 389 (2000).
[47] J. A. Elliot, J. Sandler, M. S. P. Shaffer, R. J. Young, and A. H. Windle (unpublished).
[48] J. Bernholc, C.J. Brabec, M.B. Nardelli, A. Maiti, C. Roland, and B.I. Yakobson, Appl. Phys. A: Mater. Sci. Process. **67**, 39 (1998).
[49] B.I. Yakobson, C.J. Brabec, and J. Bernholc, Phys. Rev. Lett. **76**, 2511 (1996).
[50] S. Iijima, C. Brabec, A. Maiti, and J. Bernholc, J. Chem. Phys. **104**, 2089 (1996).
[51] C.F. Cornwell and L.T. Wille, Solid State Commun. **101**, 555 (1997).
[52] B.I. Yakobson and R.E. Smalley, Am. Sci. **85**, 324 (1997).